Lifetime of spin-orbit induced spin textures in a semiconductor heterostructure probed by quantum corrections to conductivity

Takahito Saito,[1] Toshimichi Nishimura,[1] Ju-Young Yoon,[1] Jonas Kölzer,[2,3] Daisuke Iizasa,[1] Michael Kammermeier,[4,5] Thomas Schäpers,[2,3,5] Junsaku Nitta,[1,5,6] and Makoto Kohda[1,5,6,7,8,*]

[1]Department of Materials Science, Tohoku University, Sendai 980-8579, Japan
[2]Peter Grünberg Institute (PGI-9), Forschungszentrum Jülich, 52425 Jülich, Germany
[3]Jülich-Aachen Research Alliance (JARA)-Fundamentals of Future Information Technology, Forschungszentrum Jülich and RWTH Aachen University, 52425 Jülich, Germany
[4]School of Chemical and Physical Sciences and MacDiarmid Institute for Advanced Materials and Nanotechnology, Victoria University of Wellington, P.O. Box 600, Wellington 6140, New Zealand
[5]Center for Science and Innovation in Spintronics (Core Research Cluster), Tohoku University, Sendai 980-8577, Japan
[6]Center for Spintronics Research Network, Tohoku University, Sendai 980-8577, Japan
[7]Division for the Establishment of Frontier Sciences of the Organization for Advanced Studies, Tohoku University, Sendai 980-8577, Japan
[8]Quantum Materials and Applications Research Center, National Institute for Quantum Science and Technology, 1233 Watanuki, Takasaki, Gunma 370-1292, Japan

(Received 5 July 2022; revised 6 November 2022; accepted 15 November 2022; published 27 December 2022)

The persistent spin helix (PSH) is the stable spin state protected by SU(2) spin-rotation symmetry. Long-lived spin textures, referred to as helical and homogeneous spin modes, emerge as a result of this symmetry. These textures are potential candidates for the development of quantum and topological phenomena as well as information carriers in semiconductors. To this end, revealing the lifetime of all spin modes is of great importance. We experimentally reveal the lifetime of both helical and homogeneous spin modes in the vicinity of the PSH state by fully electrical means through quantum corrections to the conductivity. In a (001)-grown GaAs/AlGaAs two-dimensional electron gas, we measure the weak antilocalization in the condition where Rashba and Dresselhaus spin-orbit (SO) interactions coexist. According to the latest theory on magnetoconductance [Kammermeier *et al.*, Phys. Rev. B **104**, 235430 (2021)], the Cooperon triplet mode in the quantum corrections can be decoupled into helical and homogeneous spin modes in the vicinity of the PSH state, which allows each mode lifetime to be determined from the quantum interference effect. By using a real-space simulation in tandem with the experiment, we were able to simultaneously evaluate the relaxation rates of the two spin modes. Our results show that the ratio of Rashba and Dresselhaus SO coefficients is modulated by the top gate and that this quadratically changes the relaxation rates of the helical and homogeneous spin modes, which is consistent with theoretical predictions. These findings pave the way for exploring electron spin textures in various bandgap materials from semiconductors to metals.

DOI: 10.1103/PhysRevResearch.4.043217

I. INTRODUCTION

A better understanding of spatial spin textures is expected to usher in a set of concepts in quantum and topological phenomena in condensed matter physics. In magnetic materials, magnetic moments form various spatial structures, including noncollinear, swirling, noncoplanar, and chiral spin textures, and these are associated with the emergence of exotic topological effects and states, such as the anomalous Hall effect [1], topological Hall effect [2,3], chiral domain wall [4,5], skyrmion [6,7], and chiral-spin rotation [8]. Because of the interaction between local magnetic moments and free carriers, various ways to probe these emergent spin structures have been established through magnetoelectrical and magneto-optical effects. In nonmagnetic materials such as semiconductors, spin-orbit (SO) interaction acts as an effective magnetic field for electron spin and induces various spin textures, which also play a critical role in the realization of the coherent propagation of spin modes [9–18], the topological spin texture of electrons [19], exotic quasiparticles [20,21], and the control of light propagation [22]. Despite the emergence of these fascinating phenomena and physics, in nonmagnetic materials, the equilibrium charge population between up and down spins without local magnetic moments makes it challenging to probe these spin textures.

Two different contributions of SO effective magnetic fields are believed to play a role in the stabilization of spin textures in III–V semiconductor heterostructures: the Rashba term [23] α, which arises from structure inversion asymmetry in a

*makoto@material.tohoku.ac.jp

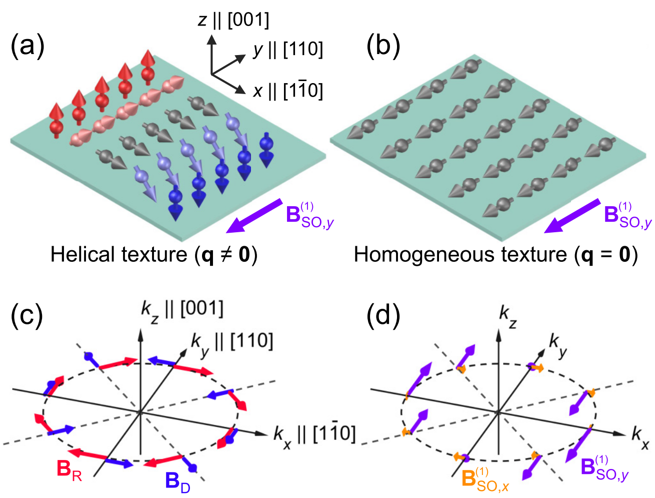

FIG. 1. Schematic view of (a) helical and (b) homogeneous spin textures. (c) Configuration of Rashba (red) and linear Dresselhaus (blue) spin-orbit (SO) field in a (001)-grown quantum well (QW). (d) Near the persistent spin helix (PSH) state, total SO field is dominated by its large y component of SO field $B^{(1)}_{\mathrm{SO},y}$ (purple) with SU(2) symmetry, while small x component $B^{(1)}_{\mathrm{SO},x}$ (orange) breaks the symmetry and cause D'yakonov-Perel' (DP) spin relaxation.

quantum well (QW), and the linear β_1 and cubic β_3 Dresselhaus terms [24], which arise from bulk inversion asymmetry in the crystal structure. While the momentum-dependent SO fields $\mathbf{B}_{\mathrm{SO}}$ cause D'yakonov-Perel' (DP) spin relaxation [25], much research attention has been focused on the situation of $|\alpha| = \beta_1 - \beta_3$ in a (001)-grown QW, the so-called persistent spin helix (PSH) state [9,10]. In this state, a uniaxial SO field with spin SU(2) symmetry generates unique spin textures which suppress DP spin relaxation [11] and enable coherent spin propagation [12]. The induced spin textures under the PSH state are classified into two modes according to the helical spin wave vector $\mathbf{q}$: the helical ($\mathbf{q} \neq 0$) and homogeneous ($\mathbf{q} = 0$) modes shown in Figs. 1(a) and 1(b) respectively, which correspond to the eigenstates of spin-diffusion equation [10,26–31]. The helical mode is a spatially rotating spin texture with a spin-rotational plane perpendicular to the uniaxial SO field [Fig. 1(a)]. The homogeneous mode is a spatially uniform spin texture along a uniaxial SO field which is developed in the plane for a (001) QW [Fig. 1(b)].

By optically exciting nonequilibrium spin polarization perpendicular to a QW plane, the evolution of the helical spin mode is observed via transient spin grating [11] and high-resolution scanning Kerr rotation microscopy [12,32–35], while the excitation of the homogeneous spin mode is difficult through the optical selection rule for a (001) QW. In the case of QWs grown along other crystal directions, the accessible spin mode varies depending on the angle between the SO field and growth direction, but only one of the spin modes is accessible under optical spin pumping [31,36]. In addition, the bandgap energy should correspond to the laser wavelength for the efficient excitation of spin-polarized electrons. This requirement limits the materials available.

In contrast, the quantum interference effect on magnetotransport is highly sensitive to spin relaxation for equilibrium spin population. This can be detected through conductance modulation by the small out-of-plane magnetic field B_z, resulting in weak localization (WL) and weak antilocalization (WAL). In the vicinity of the PSH state, the magnetic field at local minimum of magnetoconductance, denoted as B_{dip}, varies with the balance between Rashba and Dresselhaus SO field and becomes $B_{\mathrm{dip}} = 0$ at the exact PSH point, resulting in the transition from WAL to WL [13,15,37]. In this spin-related interference effect, all the initial spin states contribute to the conductance modulation. Because both the in-plane and out-of-plane components contribute, it is reasonable to assume that both the helical and homogeneous spin modes can be realized even in a (001) QW. Furthermore, because WL/WAL correction is a general phenomenon, it applies to the PSH states in various semiconductor materials. However, the relation between the WL/WAL signal and the long-lived spin textures of electrons has not yet been clarified.

Here, we establish an approach for exploring the spin textures by electrically revealing the lifetime of both helical and homogeneous spin modes in a III–V semiconductor QW. Based on the theoretical framework on the quantum corrections to magnetoconductance in the vicinity of the PSH state [38,39], we found that Cooperon triplet scattering in WAL is decoupled into helical and homogeneous spin mode contributions. This separation enables the lifetime of each spin mode to be quantitatively evaluated; this can be confirmed by real-space simulations of both quantum interference and optical spin-mode excitation. Next, we conduct magnetoconductance measurements in a (001)-grown GaAs/AlGaAs QW. The first step is to confirm the relative strength of the Rashba and Dresselhaus SO coefficients which are so close to the PSH condition by employing the anisotropic WL against in-plane external magnetic field angle in wire structures. Then, in a Hall bar device, we observe WAL signals in various gate voltages and analyze the spin-mode lifetime. The evaluated lifetime of both helical and homogeneous spin modes is in good agreement with the theoretical calculation. These results are expected to open pathways for the exploration of the long-lived spin textures which exist in various semiconductors and nonmagnetic materials but are not accessible by optical means [40–55].

II. SPATIAL SPIN TEXTURES AND QUANTUM CORRECTIONS TO CONDUCTIVITY NEAR THE PERSISTENT SPIN HELIX STATE

In a (001)-grown III–V semiconductor QW, the SO field in $x \parallel [1\bar{1}0]$ and $y \parallel [110]$ orientations is given by [Fig. 1(c)]

$$\mathbf{B}_{\mathrm{SO}} = \frac{2k}{g\mu_{\mathrm{B}}}\left\{\begin{bmatrix}(\alpha+\beta_1-\beta_3)\sin\theta\\ (-\alpha+\beta_1-\beta_3)\cos\theta\end{bmatrix} + \begin{pmatrix}\beta_3\sin 3\theta\\ -\beta_3\cos 3\theta\end{pmatrix}\right\}$$
$$= \mathbf{B}^{(1)}_{\mathrm{SO}} + \mathbf{B}^{(3)}_{\mathrm{SO}}. \quad (1)$$

Here, $g(<0)$ is the electron g factor, μ_{B} is the Bohr magneton, k is the electron wavenumber, θ is the angle of the electron momentum from the $[1\bar{1}0]$ direction, i.e., $k_x = k\cos\theta$ and $k_y = k\sin\theta$. Based on our previous result [56], we assume a Rashba coefficient of $\alpha < 0$ and define the Dresselhaus coefficients as $\beta_1 = -\gamma\langle k_z^2\rangle$ and $\beta_3 = -\gamma k_{\mathrm{F}}^2/4$ with a bulk Dresselhaus coefficient $\gamma(<0)$, a Fermi wave number k_{F}, and $\langle k_z^2\rangle$ representing the expected value of the squared wave number along the growth direction. Figure 1(d) shows the configuration of the SO field in the vicinity of the PSH state. The total $\mathbf{B}_{\mathrm{SO}}$ is slightly tilted from the uniaxial orientation parallel to k_y due to the slight imbalance between α and $\beta_1 - \beta_3$ and/or cubic Dresselhaus contributions. Nevertheless, $\mathbf{B}_{\mathrm{SO}}$ is dominated by large $B^{(1)}_{\mathrm{SO},y} = (2k/g\mu_{\mathrm{B}})(-\alpha + \beta_1 - \beta_3)\cos\theta$, which preserves spin SU(2) symmetry and only contributes to WL. This uniaxial SO field stabilizes helical and homogeneous spin modes with helical wave vectors $\mathbf{q} = (q_0,\ 0)$ and $(0,\ 0)$, respectively [Figs. 1(a) and 1(b)], in which the pitch of the helix is defined by $\lambda_0 = 2\pi/q_0$, with $q_0 = (2m^*/\hbar^2)(-\alpha + \beta_1 - \beta_3)$. In contrast, small $B^{(1)}_{\mathrm{SO},x} = (2k/g\mu_{\mathrm{B}})(\alpha + \beta_1 - \beta_3)\sin\theta$ and $\mathbf{B}^{(3)}_{\mathrm{SO}}$ break the SU(2) symmetry of the uniaxial SO field, noted as symmetry-breaking terms [38]. This results in enhanced spin relaxation and causes the WAL contribution in quantum corrections to the conductivity. The theoretical expression of the relaxation rate for helical and homogeneous spin modes are obtained from eigenvalues of spin-diffusion equation as [30,31]

$$\Gamma_{\mathrm{heli}} = 2D\frac{m^{*2}}{\hbar^4}\{[|\alpha| - (\beta_1 - \beta_3)]^2 + 3\beta_3^2\}, \tag{2a}$$

$$\Gamma_{\mathrm{homo}} = 4D\frac{m^{*2}}{\hbar^4}\{[|\alpha| - (\beta_1 - \beta_3)]^2 + \beta_3^2\}. \tag{2b}$$

Here, D is the diffusion constant, m^* is the effective mass of electron, and $\hbar$ is the reduced Planck's constant.

The quantum interference effect originating from WL and WAL sensitively detects the SO induced spin relaxation in the time-reversal symmetric path for a moving electron. Among the many related quantum correction theories which have been developed for decades, there are various types of analytical and closed-form expressions for quantitatively evaluating SO coefficients [38,39,57–63]. Near the PSH state, the closed-form expression of magnetoconductance has been developed by taking advantage of the decoupled Cooperon triplet scattering terms under collinear SO field [38]. We further formulate the simplified Cooperon spectrum by explicitly considering the lifetime of helical and homogeneous spin modes [39]. Detailed information for deriving the quantum correction to the conductivity is shown in Appendix A:

$$\Delta\sigma(B_z) = -\frac{e^2}{4\pi^2\hbar}(\tilde{\Psi}_{\mathrm{singlet}} - 2\tilde{\Psi}_{\mathrm{heli}} - \tilde{\Psi}_{\mathrm{homo}}), \tag{3a}$$

$$\tilde{\Psi}_{\mathrm{singlet}} = \Psi\left(\frac{1}{2} + \frac{B_\phi}{B_z}\right) - \ln\frac{B_{\mathrm{tr}}}{B_z}, \tag{3b}$$

$$\tilde{\Psi}_{\mathrm{heli}} = \Psi\left(\frac{1}{2} + \frac{B_\phi}{B_z} + \frac{\hbar}{4eDB_z}\Gamma_{\mathrm{heli}}\right) - \ln\frac{B_{\mathrm{tr}}}{B_z}, \tag{3c}$$

$$\tilde{\Psi}_{\mathrm{homo}} = \Psi\left(\frac{1}{2} + \frac{B_\phi}{B_z} + \frac{\hbar}{4eDB_z}\Gamma_{\mathrm{homo}}\right) - \ln\frac{B_{\mathrm{tr}}}{B_z}. \tag{3d}$$

Here, e is the elementary charge, and Ψ is the digamma function. Then $\tilde{\Psi}_{\mathrm{singlet}}$ corresponds to the Cooperon singlet mode, and $\tilde{\Psi}_{\mathrm{heli}}$ and $\tilde{\Psi}_{\mathrm{homo}}$ correspond to the decoupled Cooperon triplet modes. The characteristic fields B_ϕ and B_{tr} are given by

$$B_\phi = \frac{\hbar}{4eL_\phi^2}, \tag{4a}$$

$$B_{\mathrm{tr}} = \frac{\hbar}{2el_{\mathrm{tr}}^2}, \tag{4b}$$

with the electron phase coherence length L_ϕ, and the mean free path l_{tr}. It should be emphasized that $\tilde{\Psi}_{\mathrm{heli}}$ and $\tilde{\Psi}_{\mathrm{homo}}$ are described by the spin-relaxation rate of helical Γ_{heli} and homogeneous Γ_{homo} spin modes. This is because the eigenvalue spectrum of the spin-diffusion equation and the triplet Cooperon are identical under time-reversal symmetry in the absence of the magnetic field [27,39,64]. An intuitive picture explaining the reasons for detecting the lifetime of specific spin modes among various spin wave vectors is as follows: The PSH state stabilizes the long-lived spin texture and prolongs the lifetime of helical and homogeneous spin modes over other wave vectors. The spin interference contributing to the quantum corrections to the conductivity takes place within the length scale of the spin relaxation. Because of the large difference in spin relaxation time between the helical/homogeneous spin mode and other wave vectors, the long spin lifetime of helical and homogeneous spin modes mainly contributes to the spin interference. In the case where only Rashba or Dresselhaus are considered, the lifetime of eigen spin modes is not so different from the other wave vectors. Therefore, the averaged spin relaxation on the existing wave vectors can be determined by the SO field. Consequently, in the vicinity of the PSH state, the relaxation rate of both helical Γ_{heli} and homogeneous Γ_{homo} spin modes can be evaluated from the quantum interference effect in Eqs. (3a)–(3d). This enables us to simultaneously access both helical and homogeneous spin textures by electrical means. Note that the optical Kerr rotation approach is limited because of the difficulty in detecting both spatial spin textures at the same time [31].

III. MONTE CARLO-BASED REAL-SPACE SIMULATIONS

To confirm that the lifetime of both helical and homogeneous spin modes can be clarified through electrical means in III–V semiconductor heterostructures, we first perform two independent real-space simulations based on the Monte Carlo method. One is the WL/WAL correction established by Sawada and Koga [65], and the other is spatiotemporal spin dynamics assuming time-resolved Kerr rotation (TRKR) microscopy (detailed information of the simulation procedures are shown in Appendix B). In the model of Sawada and Koga [65], the quantum-interference amplitude is calculated for numerous closed loops up to 100 000 and converted to a magnetoconductance curve. Since this simulation captures all SO fields, near the PSH state can be simulated, and this can be achieved not only in the diffusive regime but also in the ballistic regime. We fix the following parameters for both simulations: carrier density $N_s = 3.0 \times 10^{15}\ \mathrm{m}^{-2}$, $D = 0.043\ \mathrm{m}^2/\mathrm{s}$, $L_\phi = 10\ \mu\mathrm{m}$, $\beta_1 = 2.3\,\mathrm{meV\,Å}$, and $\beta_3 = 0.40\,\mathrm{meV\,Å}$, while α is varied from -0.75 to $-5.7\,\mathrm{meV\,Å}$. In Fig. 2(a), the simulated magnetoconductance $\sigma(B_z) - \sigma(0)$ is plotted as gray circles for various $|\alpha|/(\beta_1 - \beta_3)$ ratios. These magnetoconductance curves are fitted with Eqs. (3a)–(3d), setting Γ_{heli}, Γ_{homo} and L_ϕ as fitting parameters [blue lines in Fig. 2(a)]. The WL/WAL behaviors are well described by Eqs. (3a)–(3d) in all $|\alpha|/(\beta_1 - \beta_3)$ values. In Fig. 2(d), we show the extracted mode relaxation rates Γ_{heli} and Γ_{homo} (blue and green circles, respectively) as a function of $|\alpha|/(\beta_1 - \beta_3)$, exhibiting quadratic behavior against $|\alpha|/(\beta_1 - \beta_3)$ and the minimum value at the exact PSH point $[|\alpha|/(\beta_1 - \beta_3) = 1]$.

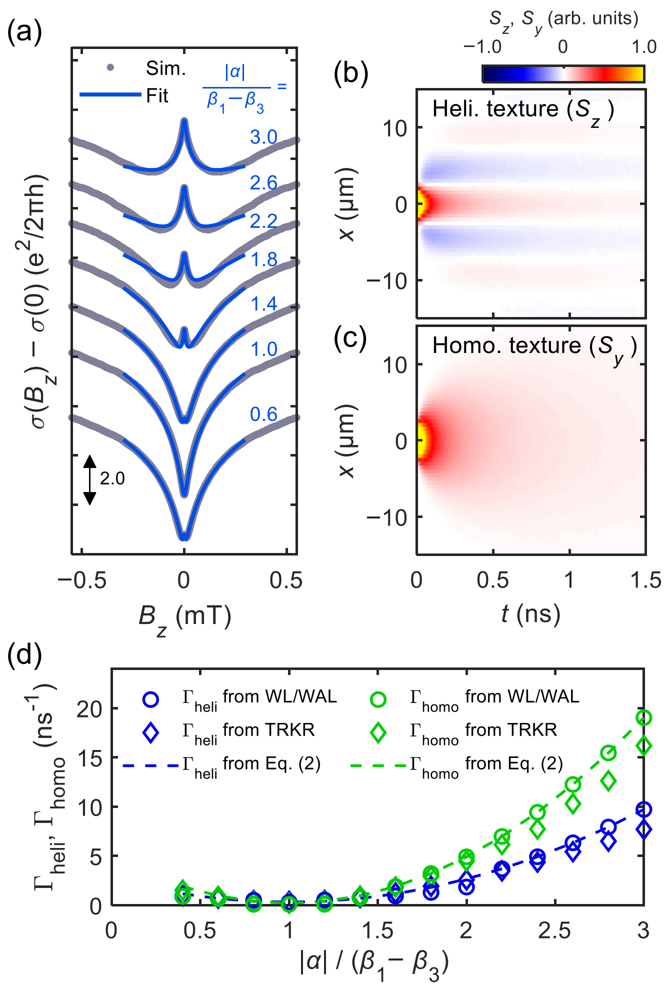

FIG. 2. (a) Real-space simulated magnetoconductance $\sigma(B_z) - \sigma(0)$ (gray) and fits with Eqs. (3a)–(3d) (blue) for various spin-orbit (SO) ratios from $|\alpha|/(\beta_1-\beta_3) = 0.6$ to 3.0. Color-scale plot of spatiotemporal evolution of (b) S_z into helical texture and (c) S_y into homogeneous texture at $|\alpha|/(\beta_1-\beta_3) = 1$ obtained by Monte Carlo simulation. (d) Relaxation rates of helical $\Gamma_{\rm heli}$ (blue) and homogeneous $\Gamma_{\rm homo}$ (green) spin textures extracted from weak localization/weak antilocalization (WL/WAL; circles), time-resolved Kerr rotation (TRKR) simulation (diamonds), and calculated from Eqs. (2a) and (2b) (dashed line) plotted as a function of $|\alpha|/(\beta_1-\beta_3)$.

This is in quantitatively good agreement with the theoretical values calculated from Eqs. (2a) and (2b) [dashed blue and green lines in Fig. 2(d)].

Next, we compare the mode relaxation rates obtained from the WL/WAL simulation to Monte Carlo–based TRKR microscopy. We initialize an ensemble of spins aligned either along the z or y direction in Fig. 1(d) to excite the helical or homogeneous spin mode, respectively. In this simulation, since one of the spin textures is selectively excited with the nonequilibrium spin population, we can directly compare the lifetime of helical and homogeneous spin modes with those evaluated from the WL/WAL simulation. Initial spins are populated at time $t = 0$ in a Gaussian distribution with the effective sigma width of $w_0 = 0.71$ μm. During the random motion of electrons, each spin precesses around the SO field within the mean scattering time $\tau = 2D/v_{\rm F}^2$, where $v_{\rm F}$ is the Fermi velocity. As shown in the color-scale plot of the spatiotemporal dynamics in Figs. 2(b) and 2(c) for $|\alpha|/(\beta_1-\beta_3) = 1.0$, the spin ensemble aligned along z (y) at $t = 0$ is developed into a helical (homogeneous) spatial texture in the x direction by the uniaxial SO field. We conduct such a spatiotemporal simulation with different α values (detailed information for simulating the spatiotemporal spin dynamics is shown in Appendix C). The mode relaxation rate is directly evaluated by fitting the spatiotemporal map with the following equations [30,31]:

$$S_z(x, y=0, t) = \frac{w_0^2}{w_0^2+2Dt}\exp\left[-\frac{x^2+2Dq_0^2w_0^2t}{2\left(w_0^2+2Dt\right)}\right] \times \exp(-\Gamma_{\rm heli}t)\cos\left(\frac{2Dt}{w_0^2+2Dt}q_0x\right), \tag{5a}$$

$$S_y(x, y=0, t) = \frac{w_0^2}{w_0^2+2Dt}\exp\left[-\frac{x^2}{2\left(w_0^2+2Dt\right)}\right] \times \exp\left(-\Gamma_{\rm homo}t\right). \tag{5b}$$

The obtained $\Gamma_{\rm heli}$ and $\Gamma_{\rm homo}$ are shown as open blue and green diamonds in Fig. 2(d), respectively, and are compared with those from the WL/WAL simulation and theoretical values. We find good agreement of $\Gamma_{\rm heli}$ and $\Gamma_{\rm homo}$ between TRKR and WL/WAL simulation for the entire range of $|\alpha|/(\beta_1-\beta_3)$. These results indicate that the helical and homogeneous spin modes simultaneously govern the spin-relaxation phenomena in WL/WAL and that the relaxation rates of these are identical with those in the TRKR simulation. This is evidence that the relaxation rates of both spin modes are electrically evaluated via WL/WAL measurement.

IV. MAGNETOCONDUCTANCE MEASUREMENTS

A. Experimental methods

In the experiment, we implemented the proposed electrical detection of the spin-mode lifetime to a 20-nm-thick GaAs/AlGaAs QW grown on a (001) GaAs substrate. The Si-doped $Al_{0.3}Ga_{0.7}As$ layer was placed at 10 nm above the GaAs QW layer to make the QW asymmetric and induce a small Rashba SO field close to the Dresselhaus SO field. We processed the wafer into the Hall bar structure with a width of 20 μm and a length of 160 μm using photo lithography and wet-chemical etching [Fig. 3(a)]. The channels were covered with a Cr (30 nm)/Au (100 nm) top gate to tune α and β_3 as well as the carrier density N_s [66]. Magnetoconductance was measured by a sweeping perpendicular magnetic field B_z and by employing the standard lock-in technique to observe the WAL at a sample temperature of $T = 0.3$ K. Modulation of carrier density through the top gate voltage was confirmed by Shubnikov–de Haas (SdH) oscillation, successfully modulating N_s from 3.6×10^{15} to 6.5×10^{15} m^{-2}. In addition to the Hall bar structure, we also fabricated the 800-nm-wide wire structure by electron beam lithography and reactive ion etching along the [010] direction [Fig. 3(b)]. This allows us to confirm that the designed QW is close to the PSH state: the α/β_1 ratio is evaluated through anisotropic WL under

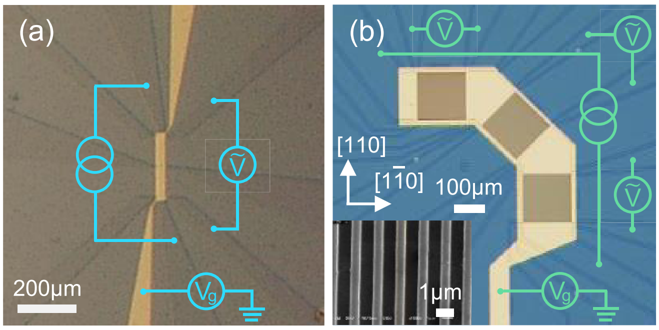

FIG. 3. Optical micrographs of (a) the Hall bar structure and (b) the parallel wire structure. (a) Magnetoconductance was measured in the Hall bar structure to demonstrate the electrical detection of the spin-mode lifetime. (b) Parallel wire structure was prepared along [1$\bar{1}$0] (left), [010] (middle), and [110] (right) orientations to measure the anisotropic weak localization behavior under in-plane external magnetic field. The [010]-oriented wire was used to evaluate the spin-orbit (SO) ratio α/β_1, as shown in the main text and Fig. 4, while the [1$\bar{1}$0]- and [110]-oriented wires were for the confirmation of the SO field direction [68,69]. Inset shows a scanning electron microscope image of parallel wire structure.

an in-plane magnetic field [67,68]. We prepared 50 parallel wires to average out the universal conductance fluctuation. The effective wire width can be evaluated from the resistance peak before starting the SdH oscillation [68,69]. Because of the carrier depletion at the sidewalls, the effective wire width is reduced to 350 nm, which is comparable with or smaller than $l_{\mathrm{tr}} = 195$ to 1250 nm in given N_s. We fix the in-plane magnetic field $B_{\mathrm{in}} = 2$ T and rotate its direction from $\theta_{\mathrm{in}} = 0^\circ$ to 180° ([1$\bar{1}$0] to [$\bar{1}$10]) and measure the magnetoconductance at $T = 1.6$ K.

B. Ratio between Rashba and Dresselhaus coefficients from anisotropic weak localization in wire structures

Since the electrical detection of the spin-mode lifetime given by Eqs. (3a)–(3d) is applicable near the PSH, we first evaluate the relative ratio between the Rashba and Dresselhaus coefficients based on the anisotropic WL behavior under in-plane external magnetic field in wire structures [67,68]. When the electron spin is laterally confined in a wire with a width narrower than the spin precession length, DP spin relaxation is suppressed due to the unidirectional $\mathbf{B}_{\mathrm{SO}}$ orientation on the quasi-one-dimensional (quasi-1D) electron momentum [70], resulting in WL in the magnetoconductance [71]. The amplitude of WL is reduced when the applied in-plane magnetic field $\mathbf{B}_{\mathrm{in}}$ breaks the unidirectional alignment of the total magnetic field, i.e., $\mathbf{B}_{\mathrm{in}} \nparallel \mathbf{B}_{\mathrm{SO}}$. Therefore, by rotating $\mathbf{B}_{\mathrm{in}}$ in different angles θ_{in}, the direction of $\mathbf{B}_{\mathrm{SO}}$ is directly extracted from the angle where the WL amplitude is maximized, i.e., $\mathbf{B}_{\mathrm{in}} \parallel \mathbf{B}_{\mathrm{SO}}$ ($\theta_{\mathrm{in}} = \theta_{\mathrm{peak}}$) [Fig. 4(a)]. In the wire oriented along the [010] axis, the Rashba $\mathbf{B}_{\mathrm{R}}$ field and linear Dresselhaus $\mathbf{B}_{\mathrm{D1}}$ field are mutually perpendicular to each other, where the $\mathbf{B}_{\mathrm{R}}$ ($\mathbf{B}_{\mathrm{D1}}$) points are perpendicular (parallel) to the wire orientation [Fig. 4(a)]. This $\mathbf{B}_{\mathrm{SO}}$ configuration enables us to evaluate the relative strength of Rashba and linear Dresselhaus

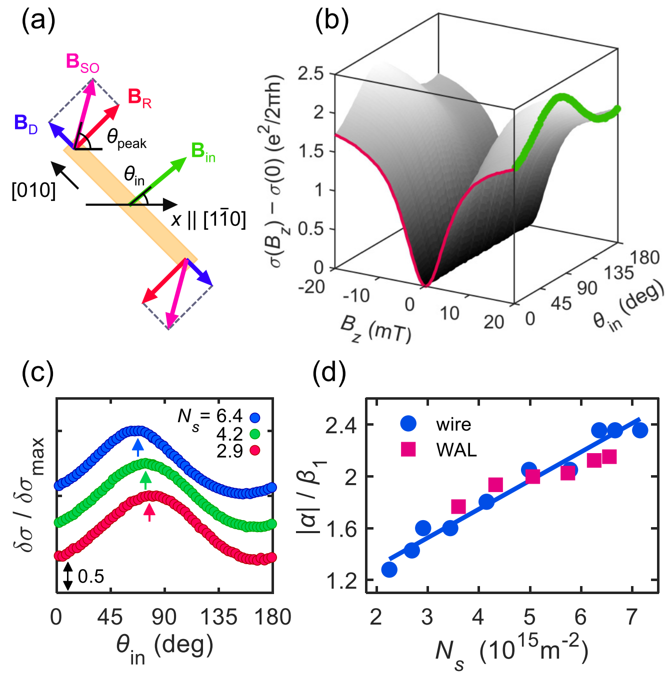

FIG. 4. (a) Schematic orientation of Rashba (red), Dresselhaus (blue), and total spin-orbit (SO) field (pink) and in-plane external magnetic field (green) for [010]-oriented wire. (b) Three-dimensional plot of magnetoconductance $\sigma(B_z) - \sigma(0)$ in [010]-oriented wire structure for various angles of in-plane magnetic field θ_{in} at gate voltage $V_g = 0.0$ V ($N_s = 4.2 \times 10^{15}$ m^{-2}). (c) Weak localization (WL) amplitude $\delta\sigma = \sigma(B_z = 20\text{ mT}) - \sigma(0)$ is normalized by its maximum $\delta\sigma_{\mathrm{max}}$ and plotted $(\delta\sigma/\delta\sigma_{\mathrm{max}})$ as a function of θ_{in} for carrier densities $N_s = 2.9$, 4.2, and 6.4×10^{15} m^{-2}. Each signal is vertically shifted for clarity. (d) The ratio between Rashba and linear Dresselhaus SO coefficients $|\alpha|/\beta_1$ as a function of N_s evaluated from wire measurement (blue) and from SO coefficients on weak antilocalization (WAL) analysis (pink). In wires, considering that $45^\circ < \theta_{\mathrm{peak}} < 90^\circ$, $\alpha < 0$ and $|\alpha| > \beta_1$ are obtained in measured V_g range. The blue solid line shows the linear assumption of $|\alpha|/\beta_1$ against N_s [$|\alpha|/\beta_1 = R(N_s) = AN_s + C$].

field α/β_1, as simply described in [68,69,72],

$$\frac{\alpha}{\beta_1} = -\cot(\theta_{\mathrm{peak}} - 45^\circ). \tag{6}$$

The θ_{peak} is defined from the [1$\bar{1}$0] axis. It should be noted that, because the first- and third-harmonic β_3 terms cancel each other out in the [010] orientation ($\theta = 135^\circ$), the SO field is given with only α and β_1 [see Eq. (1)].

Figure 4(b) shows the three-dimensional plot of the obtained magnetoconductance $\sigma(B_z) - \sigma(0)$ in various θ_{in} at $V_g = 0.0$ V ($N_s = 4.2 \times 10^{15}$ m^{-2}). The signals show WL (the pink solid line), indicating the suppression of DP relaxation due to the lateral confinement. In addition, anisotropic behavior is clearly observed in the WL amplitude against θ_{in} (green curves). We conducted the same analysis in Fig. 4(b) between $N_s = 2.3 \times 10^{15}$ and 7.2×10^{15} m^{-2} by changing the top gate voltage. In Fig. 4(c), the WL amplitude $\delta\sigma = \sigma(B_z = 20\text{ mT}) - \sigma(0)$ is normalized by its maximum $\delta\sigma_{\mathrm{max}}$ and plotted $(\delta\sigma/\delta\sigma_{\mathrm{max}})$ as a function of θ_{in} in different N_s.

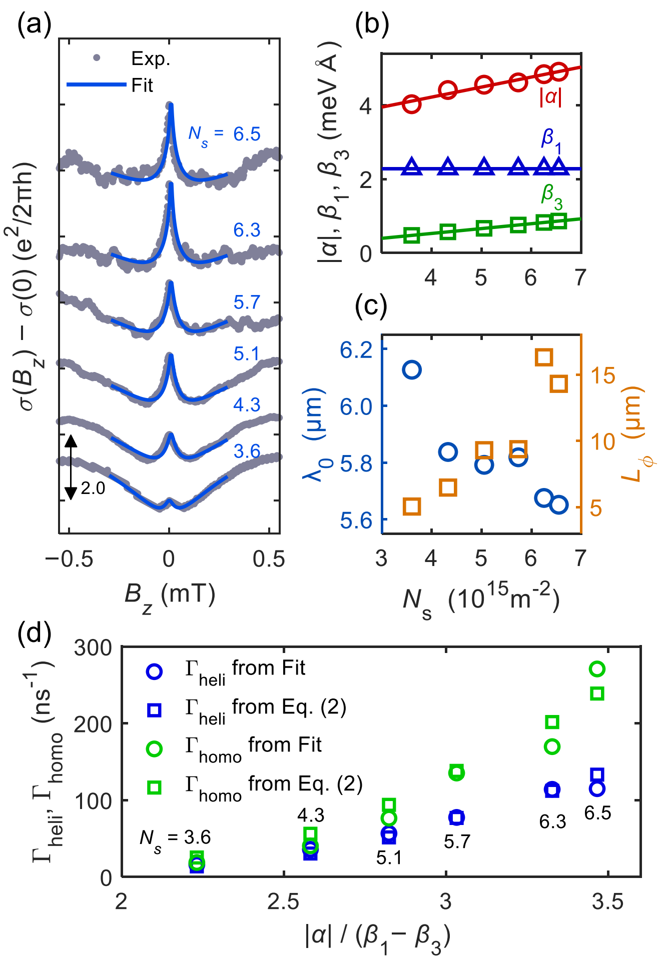

FIG. 5. (a) Measured magnetoconductance $\sigma(B_z) - \sigma(0)$ (gray) and fits with Eqs. (3a)–(3d) (blue) for various carrier densities from $N_s = 3.6$ to 6.5×10^{15} m^{-2}. (b) Full spin-orbit (SO) coefficients $|\alpha|$, β_1, and β_3 as a function of N_s evaluated via weak antilocalization (WAL) analysis in combination with wire measurement. (c) Pitch of the helical texture λ_0 (blue) and phase coherence length L_ϕ (orange) plotted against N_s. (d) Relaxation rates of helical Γ_{heli} (blue) and homogeneous Γ_{homo} (green) spin textures extracted from the fitting of WAL with Eqs. (3a)–(3d) (circles) and calculated from SO coefficients using Eqs. (2a) and (2b) (square) plotted as a function of $|\alpha|/(\beta_1 - \beta_3)$. The labeled numerals show the corresponding N_s.

The position of θ_{peak} satisfying $\mathbf{B}_{in} \parallel \mathbf{B}_{SO}$ clearly shifts with N_s [arrows in Fig. 4(c)], indicating the gate modulation of the $|\alpha|/\beta_1$ ratio. As shown in the blue circles in Fig. 4(d), the obtained $|\alpha|/\beta_1$ based on Eq. (6) varies linearly to N_s from $|\alpha|/\beta_1 = 1.28$ to 2.36, close enough to the PSH state ($|\alpha|/\beta_1 = 1$). The $|\alpha|/\beta_1$ ratio can be expressed as $|\alpha|/\beta_1 = R(N_s) = AN_s + C$ by assuming that α is linearly modulated against N_s, where $A = 0.22 \times 10^{-15}$ m^2 and $C = 0.86$ [the solid line in Fig. 4(d)].

C. Spin-mode lifetime probed by weak antilocalization measurement

Then we explore the spin-mode lifetime through WAL in a Hall bar device. In Fig. 5(a), we plot the measured magnetoconductance $\sigma(B_z) - \sigma(0)$ (gray circles) with various carrier densities N_s, where the WAL signal is weakened as N_s decreases. This is understood from Fig. 4(d) because the $|\alpha|/\beta_1$ ratio reaches 1 as N_s becomes lower, corresponding to the transient regime from WAL to WL due to suppressed spin relaxation near the PSH state. We fit the experimental WAL with magnetoconductance correction $\Delta\sigma(B_z)$ described by the spin-mode relaxation rate in Eqs. (3a)–(3d) and show the results as blue solids in Fig. 5(a). The WAL fit shows good agreement with the obtained experiment. The corresponding relaxation rate for helical and homogeneous spin modes, Γ_{heli} and Γ_{homo}, are extracted (the blue and green circles, respectively) in Fig. 5(d). The $|\alpha|/(\beta_1 - \beta_3)$ in the horizontal axis of Fig. 5(d) will be discussed and quantitatively evaluated later in Fig. 5(b). The value for Γ_{homo} is higher by a factor of two than that for Γ_{heli}, which is consistent with Eqs. (2a) and (2b), and the quadratic dependence to the Rashba coefficient α is well reproducible. These features capture the expected dependence of the mode relaxation rate simulated in Fig. 2(d) and strongly indicate that the helical and homogeneous spin modes govern the WAL phenomena near the PSH state. It should be noted that the largest contribution to the quantum interference correction is always given by the longest-lived spin states described by eigenvalues of the spin-diffusion equation. Near the PSH state, these spin states correspond to helical and homogeneous spin modes whose spin textures are well defined and stably exist. However, it should be noted that these spin states have a much shorter lifetime and a different texture when they exist far from the PSH state, where there is only the Rashba or Dresselhaus SO field, for example.

To further confirm the accuracy of the obtained mode relaxation rates, we quantitatively evaluate Rashba and Dresselhaus coefficients for the theoretical Γ_{heli} and Γ_{homo}. Evaluating all SO coefficients in the vicinity of the PSH is not straight forward due to multiple variables for fitting with quantum correction theory, involving ambiguity for extracted SO coefficients. To avoid this, we use the $|\alpha|/\beta_1$ ratio of the wire to replace $|\alpha|$ with $R(N_s)\beta_1$ in Fig. 4(d) and evaluate the bulk Dresselhaus coefficient γ (<0) from the entire WAL results in a Hall bar (details of the fitting procedure are shown in Appendix D). We obtain $\gamma = -8.4\,\mathrm{eV\,Å}^3$, which is consistent with the previous results [17,56]. Next, we fit the individual WAL data with $|\alpha|$ and L_ϕ as free fit parameters for each N_s while keeping $\gamma = -8.4\,\mathrm{eV\,Å}^3$ as a constant (details of the fitting procedure are shown in Appendix D). All the SO coefficients ($|\alpha|$, β_1, β_3) can be fully evaluated, as summarized in Fig. 5(b), where $|\alpha|$ and β_3 increase almost linearly with increasing N_s, while β_1 remains constant. Figure 5(c) shows the pitch of the helical texture $\lambda_0 = 2\pi/q_0 = (\pi\hbar^2/m^*)/(-\alpha + \beta_1 - \beta_3)$ calculated from SO coefficients, together with the phase coherence length L_ϕ. These SO coefficients in Fig. 5(b) are consistent with the values from the wire measurement by comparing the $|\alpha|/\beta_1$ ratio (the pink squares) in Fig. 4(d). By confirming that the SO coefficients are successfully obtained, the theoretical values of mode relaxation rates are calculated using Eqs. (2a) and (2b) and are plotted as open blue and green squares in Fig. 5(d). The relaxation rate of helical and homogeneous spin modes revealed from WAL in Eqs. (3a)–(3d) is quantitatively in good agreement with the theoretically expected values for the whole N_s range. These results strongly indicate that both helical and homogeneous spin modes are reliably evaluated through WAL analysis in magnetotransport measurements.

The above discussion on the lifetime of spatial spin textures is also applicable in the previously reported magnetoconductance results such as Refs. [15,38]. In these results, Rashba coefficient α and carrier density (i.e., cubic Dresselhaus coefficient β_3) are independently tuned through top and back gates in GaAs QWs, and the clear transition from WAL to WL due to strongly suppressed spin relaxation is observed around the exact PSH point. When the SO field reaches the exact PSH point ($|\alpha| = \beta_1 - \beta_3$), corresponding to that the cubic Dresselhaus term becomes dominant in total spin relaxation phenomena, the crossover of two spin-mode relaxation rates from $\Gamma_{\mathrm{heli}} < \Gamma_{\mathrm{homo}}$ to $\Gamma_{\mathrm{heli}} > \Gamma_{\mathrm{homo}}$ would be expected [see Eqs. (2a) and (2b)]. For a reliable parameter fitting, however, it is desirable that the electron phase coherence time is still larger than the spin-mode lifetime so that the WAL appears in the magnetoconductance signal.

V. OUTLOOK AND CONCLUSION

In this paper, we experimentally clarify the relation between the magnetoconductance signal and the helical and homogeneous spin mode in the vicinity of PSH state. These results incite an interpretation of WL/WAL correction to the conductivity based on the long-lived spatial electron spin textures. The spatial spin textures are fundamental features for further understanding of spintronic, quantum, and topological phenomena in condensed matter physics. Previously, these spin textures in nonmagnetic semiconductor heterostructures have been mainly investigated in optically spin-polarized electron packet. Our results on electrical evaluation of the spin-mode lifetime indicates that the long-lived spatial spin textures play an important role not only in spin-polarized electron ensemble but even in the equilibrium electron spin population without any spin polarization such as those in magnetoconductance measurement. This approach enables us to simultaneously access both helical and homogeneous spin modes. Moreover, since it does not require any optical measurement, it is applicable in many different materials.

Promising candidates for applying this approach are the narrow bandgap semiconductor heterostructures, e.g., InGaAs [13,37], InAs [40], and InSb [41,42]. Because of the small bandgap, optical excitation of nonequilibrium electron spin polarization is difficult in these materials. In addition, recently, the existence of the PSH state was theoretically predicted in a number of materials such as $LaAlO_3/SrTiO_3$ interface [43], wurtzite nanowires [18,44], ferroelectric thin films [45–49], ferroelectric oxide materials [50–52], and other materials discussed in Refs. [53,54]. The electrical switching of the PSH at room temperature is demonstrated using the circular photogalvanic effect in a van der Waals ferroelectric halide perovskite in Ref. [55]. We envision a possibility to explore the long-lived spatial spin textures in these materials by employing the experimental approach of WL/WAL measurement discussed in this paper.

In conclusion, we revealed the lifetime of the long-lived spin textures in the vicinity of the PSH state by the quantum corrections to the conductivity in a (001)-grown III–V semiconductor heterostructure. We first performed the real-space simulations of magnetoconductance correction and spatiotemporal spin dynamics assuming TRKR microscopy. Both helical and homogeneous spin modes governed the WAL, whose mode lifetimes are identical to the spin-relaxation time in the TRKR simulation. Next, we conducted the magnetoconductance measurement to analyze WAL in a (001)-grown GaAs/AlGaAs two-dimensional (2D) electron gas. Based on the discussion in the real-space simulations, the mode relaxation rates of helical and homogeneous spin modes are experimentally evaluated. A quantitative agreement of the obtained mode relaxation rates with those theoretically calculated from SO coefficients confirms that we reliably reveal the lifetime of SO induced spin textures by electrical means. Since this approach allows access to the long-lived spin textures without requiring any optical measurements, it can be applied to various semiconductors and nonmagnetic materials [40–55].

ACKNOWLEDGMENTS

We would like to thank Prof. D. C. Marinescu, Prof. J. C. Egues, Prof. T. Koga, Prof. S. Karube and Prof. C. Zhang for the insightful comments and discussions. T.Sa., T.N., D.I., M.Ko., and J.N. are supported via a Grant-in-Aid for Scientific Research (Grant No. 21H04647) by the Japan Society for the Promotion of Science. This paper was also supported by the JST FOREST Program (Grant No. JPMJFR203C2020). T.Sa., D.I., and J.-Y.Y. acknowledge the financial support from the Graduate Program in Spintronics at Tohoku University. M.Ka. acknowledges the support by the Marsden Fund Council from New Zealand government funding (Contract No. VUW1713), managed by the Royal Society Te Apārangi, and the support by the Center for Science and Innovation in Spintronics at Tohoku University, Japan.

APPENDIX A: DERIVATION OF MAGNETOCONDUCTANCE CORRECTION DESCRIBED BY THE LIFETIME OF HELICAL AND HOMOGENOUS SPIN MODES

In the diffusive regime, the quantum correction to the conductivity is described by using the Cooperon singlet and triplet scattering terms [39,73]:

$$\Delta\sigma = -\frac{e^2 D}{2\pi^2\hbar}\int_0^{2\pi}\frac{d\theta}{2\pi}\int_0^{1/\sqrt{D\tau}} q\,dq\left[-\frac{1}{E_0(\mathbf{q})} + \sum_{i=1}^{3}\frac{1}{E_i(\mathbf{q})}\right]. \tag{A1}$$

Here, D is the diffusion constant, τ is the mean scattering time, and $\mathbf{q} = (q_x,\ q_y) = q(\cos\theta, \sin\theta)$ is the wave vector. The singlet eigenvalue E_0 is given by

$$E_0 = Dq^2 + \frac{1}{\tau_\phi}. \tag{A2}$$

The triplet eigenvalues E_i ($i = 1, 2, 3$) are sensitive to the SO field. Near the PSH state with $-\alpha \approx \beta_1 - \beta_3$, the triplet scattering modes can be decoupled, and their eigenvalues are

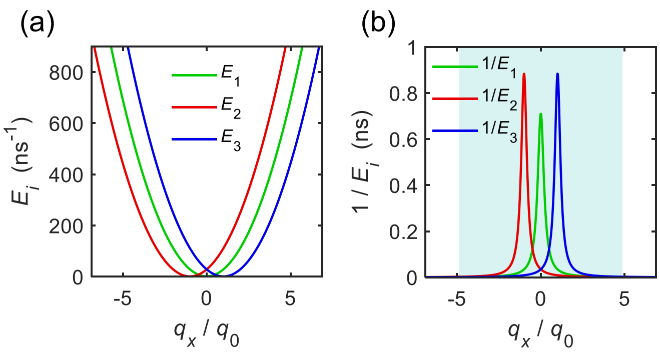

FIG. 6. (a) The Cooperon triplet eigenvalues E_i ($i = 1, 2, 3$) and (b) their inverse $1/E_i$ as functions of the wave vector ratio q_x/q_0 at Rashba coefficient $\alpha = -2.7$ meV Å and Dresselhaus coefficients $\beta_1 = 2.3$ meV Å, $\beta_3 = 0.40$ meV Å.

approximated by three parabolic functions:

$$E_1 = Dq_x^2 + Dq_y^2 + \frac{1}{\tau_\phi} + \Gamma_{\text{homo}} = Dq^2 + \frac{1}{\tau_\phi} + \Gamma_{\text{homo}}, \tag{A3a}$$

$$E_{2,3} = D(q_x \pm q_0)^2 + Dq_y^2 + \frac{1}{\tau_\phi} + \Gamma_{\text{heli}}. \tag{A3b}$$

As shown in Fig. 6(a), E_1 shows its minimum Γ_{homo} at $q = 0$, while $E_{2,3}$ show their minima Γ_{heli} at $q_x = \mp q_0$, respectively, which correspond to the relaxation rates of helical and homogeneous spin modes. It is worth noting that the Cooperon is closely related to the spin-diffusion equation [27,39]. In Fig. 6(b), the inverse of the eigenvalues $1/E_i$ are plotted with the integration range of Eq. (A1) (color-shaded in light blue). In the diffusive regime ($q_0 \ll 1/\sqrt{D\tau}$), the entire peak region is inside the integration range, and the calculation result is insensitive to the peak shift of $\pm q_0$ in $E_{2,3}$. This assumption enables us to neglect this wave vector shift and simplify the expression of $E_{2,3}$ in Eq. (A3b):

$$E_{2,3} \approx Dq_x^2 + Dq_y^2 + \frac{1}{\tau_\phi} + \Gamma_{\text{heli}} = Dq^2 + \frac{1}{\tau_\phi} + \Gamma_{\text{heli}}. \tag{A4}$$

When the perpendicular magnetic field B_z is applied, $\mathbf{q}$ becomes no longer continuous due to the Landau quantization; it is important to consider this for accurate modeling of the WAL [39]. Therefore, we replace the integral over q in Eq. (A1) by the sum over Landau level n:

$$\frac{1}{2\pi}\int_0^{1/\sqrt{D\tau}} q dq \rightarrow \frac{1}{4\pi}\frac{4eB_z}{\hbar}. \tag{A5}$$

Here, we use the relation $q^2 = (4eB_z/\hbar)(n + 1/2)$. The upper cut-off of the sum is $n_m = \hbar/(4eB_z D\tau) = B_{\text{tr}}/B_z$. By substituting Eq. (A5) into Eq. (A1), we obtain

$$\Delta\sigma = -\frac{e^2 D}{4\pi^2\hbar}\frac{4eB_z}{\hbar}\sum_{n=0}^{n_m}\left(-\frac{1}{E_{n,0}} + \sum_{i=1}^{3}\frac{1}{E_{n,i}}\right). \tag{A6}$$

The Cooperon singlet and triplet eigenvalues in Eqs. (A2)–(A4) are also rewritten using n as

$$E_{n,0} = \frac{4eDB_z}{\hbar}\left[\left(n + \frac{1}{2}\right) + \frac{B_\phi}{B_z}\right], \tag{A7}$$

and

$$E_{n,1} = \frac{4eDB_z}{\hbar}\left[\left(n + \frac{1}{2}\right) + \frac{B_\phi}{B_z} + \frac{\hbar}{4eDB_z}\Gamma_{\text{homo}}\right], \tag{A8a}$$

$$E_{n,2} = E_{n,3} = \frac{4eDB_z}{\hbar}\left[\left(n + \frac{1}{2}\right) + \frac{B_\phi}{B_z} + \frac{\hbar}{4eDB_z}\Gamma_{\text{heli}}\right]. \tag{A8b}$$

From Eq. (A6) to Eqs. (A8a) and (A8b) and the relation $\sum_{n=0}^{n_m} 1/(n + a) = -\Psi(a) + \ln n_m$, the final expressions of the magnetoconductance shown in Eqs. (3a)–(3d) are derived:

$$\Delta\sigma(B_z) = -\frac{e^2}{4\pi^2\hbar}(\tilde{\Psi}_{\text{singlet}} - 2\tilde{\Psi}_{\text{heli}} - \tilde{\Psi}_{\text{homo}}), \tag{A9a}$$

$$\tilde{\Psi}_{\text{singlet}} = \Psi\left(\frac{1}{2} + \frac{B_\phi}{B_z}\right) - \ln\frac{B_{\text{tr}}}{B_z}, \tag{A9b}$$

$$\tilde{\Psi}_{\text{heli}} = \Psi\left(\frac{1}{2} + \frac{B_\phi}{B_z} + \frac{\hbar}{4eDB_z}\Gamma_{\text{heli}}\right) - \ln\frac{B_{\text{tr}}}{B_z}, \tag{A9c}$$

$$\tilde{\Psi}_{\text{homo}} = \Psi\left(\frac{1}{2} + \frac{B_\phi}{B_z} + \frac{\hbar}{4eDB_z}\Gamma_{\text{homo}}\right) - \ln\frac{B_{\text{tr}}}{B_z}. \tag{A9d}$$

Equations (A9a)–(A9d) are a (001)-QW case of the general quantum correction model near the PSH state in Ref. [39], and it is also equivalent to the expression derived by Weigele *et al.* [38].

As shown in Fig. 7, the total magnetoconductance curve $\Delta\sigma(B_z)$ (black bold) consists of three terms: a singlet term $-e^2\tilde{\Psi}_{\text{singlet}}/4\pi^2\hbar$ (orange), a triplet helical term $2e^2\tilde{\Psi}_{\text{heli}}/4\pi^2\hbar$ (blue), and a triplet homogeneous term $e^2\tilde{\Psi}_{\text{homo}}/4\pi^2\hbar$ (green). The factor 2 in the helical term is because this term corresponds to two Cooperon triplet eigenvalues E_2 and E_3. As out-of-plane magnetic field B_z increases, the singlet term reduces the conductivity, while the triplet terms enhance the conductivity. The total magnetoconductance signal is determined by the balance between these contributions. In the exact PSH point [$|\alpha|/(\beta_1 - \beta_3) = 1.0$] [Fig. 7(a)], the triplet contribution outweighs the singlet contribution in the whole B_z range and shows WL in the quantum correction to the conductivity. When the SO ratio shifts to $|\alpha|/(\beta_1 - \beta_3) = 2.0$ [Fig. 7(b)] and 3.0 [Fig. 7(c)], the contributions of triplet terms become small due to large spin-relaxation rates Γ_{heli}, Γ_{homo}. This results in the local minimum of magnetoconductance at $B_z \neq 0$, showing WAL. Consequently, we conclude that both the helical and homogeneous spin modes govern the quantum-interference phenomena near the PSH state.

APPENDIX B: MONTE CARLO–BASED REAL-SPACE SIMULATION OF THE MAGNETOCONDUCTANCE CORRECTION

The Monte Carlo–based simulation method of WL/WAL was established by Sawada and Koga [65]. This method is a powerful tool to simulate the WL/WAL phenomena because it can include all SO fields and is applicable in both diffusive and ballistic regimes. The simulation procedure starts with the preparation of closed-loop paths of an electron by the pseudorandom number generator assuming a Boltzmannian picture. The number of scatterings required for the electron

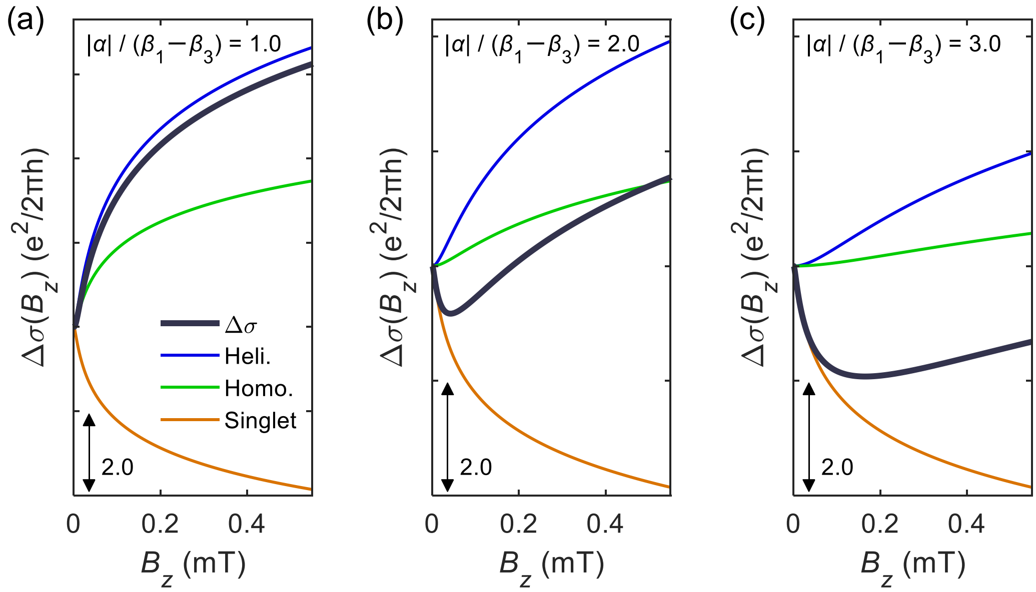

FIG. 7. The magnetoconductance $\Delta\sigma(B_z)$ obtained by Eqs. (3a)–(3d) in the main text (black bold) and its singlet term $-e^2\tilde{\Psi}_{\text{singlet}}/4\pi^2\hbar$ (orange), triplet helical term $2e^2\tilde{\Psi}_{\text{heli}}/4\pi^2\hbar$ (blue), and triplet homogeneous term $e^2\tilde{\Psi}_{\text{homo}}/4\pi^2\hbar$ (green) for (a) $|\alpha|/(\beta_1 - \beta_3) = 1.0$, (b) 2.0, and (c) 3.0.

to return in each path n_{scat} is set to $n_{\text{scat}} \leqslant N_{\text{scat}} = 5000$. The number of prepared closed loops is $N_{\text{loop}} = 100000$. Next, we calculate the quantum interference in each closed-loop path. Figure 8 exemplarily shows the jth loop of electron trajectory with $n_{\text{scat}} = 5$. This consists of line segments $\overrightarrow{l_m} = l_m(\cos\phi_m, \sin\phi_m)$ with $m = 1, 2, \ldots, 5$, where l_m and ϕ_m are the ballistic length and the momentum angle from the x axis at the mth scattering event, respectively. The quantum-interference amplitude x_j of this trajectory is expressed as

$$x_j = \exp\left(-\frac{L_j}{L'_\phi}\right)\frac{1}{2}\text{Tr}\{\mathbf{R}_{\text{tot}}^2\}(1 + \cos\phi'_j), \tag{B1}$$

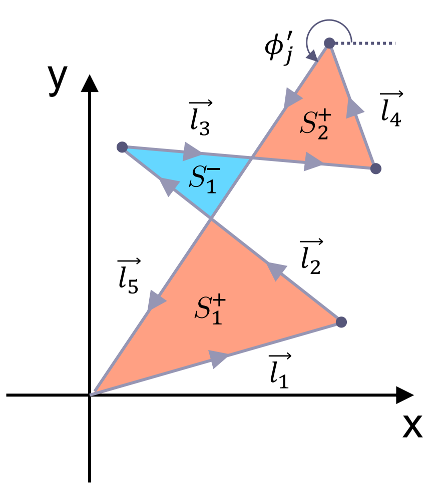

FIG. 8. The jth closed loop of electron trajectory with the number of scatterings $n_{\text{scat}} = 5$. This consists of line segments $\overrightarrow{l_m}$ with $m = 1, 2, \ldots, 5$. The encircling area S_j is given by $S_j = |S_1^+ + S_2^+ - S_1^-|$ when S_1^+, S_2^+, and S_1^- are defined to be positive.

Here, $L_j = \sum_{m=1}^{n_{\text{scat}}} l_m$ is the total length of the trajectory, $L'_\phi = v_F\tau_\phi$ is the phase coherence length, and $\phi'_j = \phi_{n_{\text{scat}}}$ is the azimuthal angle for the returning electron. Then Tr{**A**} is the trace of matrix **A**. The total spin rotation operator $\mathbf{R}_{\text{tot}}$ is calculated by [74]

$$\mathbf{R}_{\text{tot}} = \mathbf{R}_{n_{\text{scat}}} \times \mathbf{R}_{n_{\text{scat}}-1} \cdots \times \mathbf{R}_m \times \cdots \times \mathbf{R}_2 \times \mathbf{R}_1, \tag{B2}$$

with

$$\mathbf{R}_m = \begin{pmatrix} \cos\frac{Q_{\text{tot}}l_m}{2} & -i\frac{Q_x - iQ_y}{Q_{\text{tot}}}\sin\frac{Q_{\text{tot}}l_m}{2} \\ -i\frac{Q_x + iQ_y}{Q_{\text{tot}}}\sin\frac{Q_{\text{tot}}l_m}{2} & \cos\frac{Q_{\text{tot}}l_m}{2} \end{pmatrix}, \tag{B3a}$$

$$Q_{\text{tot}} = \sqrt{Q_x^2 + Q_y^2}. \tag{B3b}$$

The SO wave numbers Q_x and Q_y at (001) QW are described by

$$Q_x = (Q_\alpha + Q_\beta)\sin\phi_m + Q_{\beta 3}\sin 3\phi_m, \tag{B4a}$$

$$Q_y = (-Q_\alpha + Q_\beta)\cos\phi_m + Q_{\beta 3}\cos 3\phi_m. \tag{B4b}$$

with $Q_\alpha = 2m\alpha/\hbar^2$, $Q_\beta = 2m(\beta_1 - \beta_3)/\hbar^2$, and $Q_{\beta 3} = 2m\beta_3/\hbar^2$. Based on the quantum-interference amplitude x_j for each electron trajectory, the magnetoconductance is calculated by the following equation:

$$\Delta\sigma(B_z) = -\frac{e^2}{2\pi^2\hbar}\left(\sum_{n=3}^{N_{\text{scat}}}\frac{1}{n-2}\right)\frac{1}{N_{\text{loop}}}\sum_{j=1}^{N_{\text{loop}}} x_j\cos\left(\frac{B_z}{B_{\text{tr}}}S_j\right). \tag{B5}$$

Here, $B_{\text{tr}} = \hbar/(2el_{\text{tr}}^2)$ is the transport field, l_{tr} is the mean free path, and S_j is the encircling area for each closed trajectory.

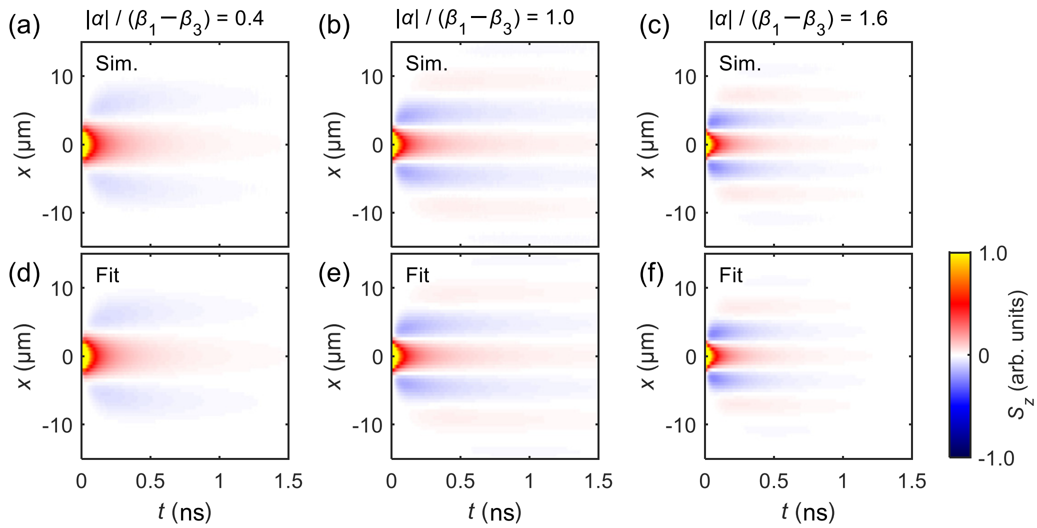

FIG. 9. Color-scale plots of spatiotemporal evolution of S_z into helical textures obtained by the Monte Carlo simulation for (a) $|\alpha|/(\beta_1-\beta_3)=0.4$, (b) 1.0, and (c) 1.6, respectively. (d)–(f) Corresponding fits of S_z to (a)–(c) using Eq. (5a) in the main text.

APPENDIX C: SIMULATION OF SPATIOTEMPORAL SPIN DYNAMICS

The spin-mode relaxation rates obtained from WL/WAL simulation are validated by comparing with the Monte Carlo–based spatiotemporal spin dynamics simulation, which corresponds TRKR microscopy. We initialize an ensemble of spins aligned either along the z or y direction at time $t=0$ in a Gaussian distribution with the effective sigma width of $w_0=0.71$ µm. The semiclassical random walk model of electron is employed with isotropic scattering on the Fermi circle, which is characterized by the mean scattering time $\tau=2D/v_{\mathrm{F}}^2=1.52$ ps with the Fermi velocity v_{F}. Dresselhaus SO coefficient $\beta_1=2.3$ meV Å and $\beta_3=0.40$ meV Å are fixed, while the Rashba SO coefficient α is varied from -0.75 to -5.7 meV Å. Each electron spin $\mathbf{s}$ moves with v_{F} between scattering events and precesses about the SO field $\mathbf{B}_{\mathrm{SO}}$ following

$$\frac{\partial}{\partial t}\mathbf{s}=\frac{g\mu_{\mathrm{B}}}{\hbar}\mathbf{B}_{\mathrm{SO}}\times\mathbf{s}. \tag{C1}$$

Because $\alpha<0$ and $|\alpha|\approx\beta_1-\beta_3$ in this paper, $\mathbf{B}_{\mathrm{SO}}$ is dominated by its large y component [see Eq. (1) and Fig. 1(d)], which preserves spin SU(2) symmetry and stabilizes the spatial spin textures. The spin ensemble initialized along the z direction starts to precess within x-z plane and evolves into the helical mode, while the spin ensemble initialized along the y direction is pinned to the y axis and forms the homogeneous mode [see Figs. 1(a) and 1(b)]. It should be noted that, in the TRKR experiment, only the out-of-plane (z) component (i.e., the helical mode) is accessible. Here, we examine both z and y components in TRKR simulation because spin-relaxation rates obtained in WL/WAL simulation are helical (z) and homogenous (y) spin textures. We locally detect the spin

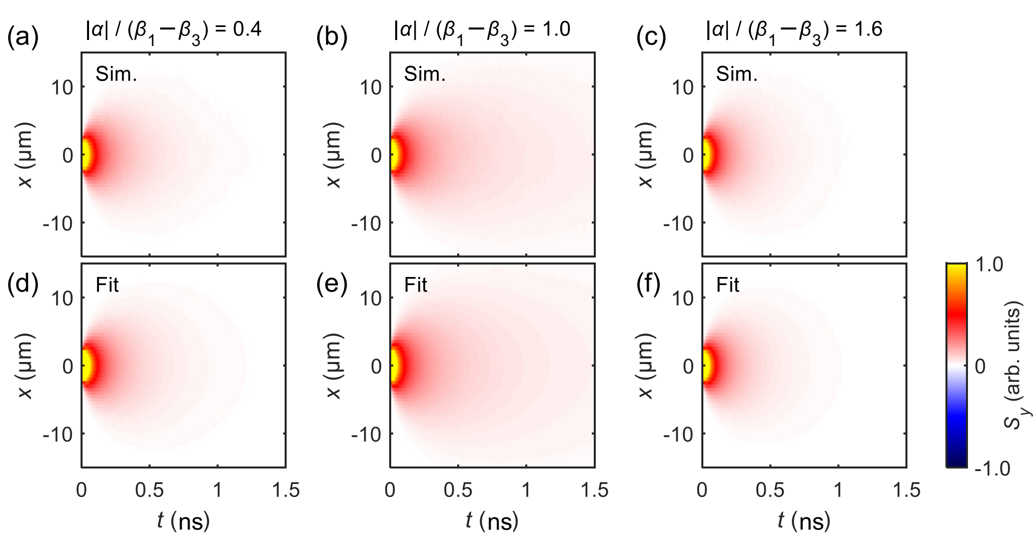

FIG. 10. Color-scale plots of spatiotemporal evolution of S_y into homogeneous textures obtained by Monte Carlo simulation for (a) $|\alpha|/(\beta_1-\beta_3)=0.4$, (b) 1.0, and (c) 1.6, respectively. (d)–(f) Corresponding fits of S_y to (a)–(c) using Eq. (5b) in the main text.

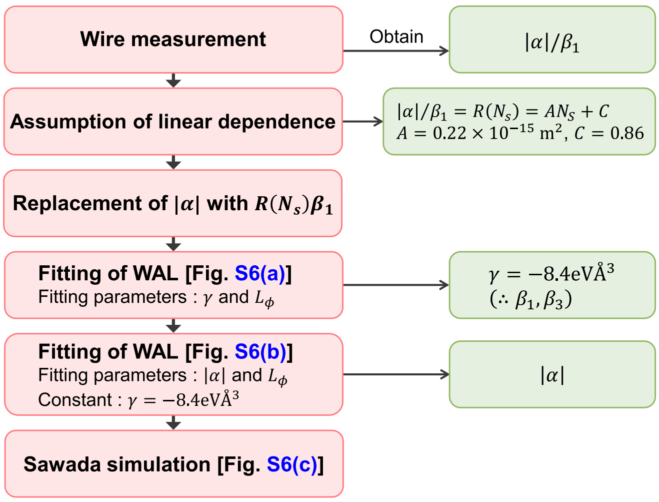

FIG. 11. Flowchart of the extraction of full spin-orbit (SO) coefficients from experimental weak antilocalization (WAL) results by combination of wire measurement.

projection and density at varying time delay t, and the spatiotemporal dynamics of the two spatial textures are observed.

Figures 9(a)–9(c) show the color-scale plots of spatiotemporal evolution of the helical texture for $|\alpha|/(\beta_1 - \beta_3) =$ 0.4, 1.0, and 1.6, respectively. As $|\alpha|$ increases with fixed β_1 and β_3, the pitch of the precession becomes shorter as the spin wave vector $q_0 = (2m/\hbar^2)(-\alpha + \beta_1 - \beta_3)$ increases monotonically, while the spin relaxation is mostly suppressed at $|\alpha|/(\beta_1 - \beta_3) = 1$, corresponding to the exact PSH state. In Figs. 10(a)–10(c), the spatiotemporal evolutions of homogeneous spin texture are plotted. In analogy to the helical spin mode, the spin-relaxation time becomes the longest at $|\alpha|/(\beta_1 - \beta_3) = 1$. These spatiotemporal maps are fitted with Eqs. (5a) and (5b) to evaluate the mode relaxation rates Γ_{heli} and Γ_{homo}. As shown in Figs. 9(d)–9(f) for the helical mode and in Figs. 10(d)–10(f) for the homogeneous mode, Eqs. (5a) and (5b) reproduce the precession and relaxation behavior very well. The obtained mode relaxation rates are plotted and compared with those from WL/WAL simulation in Fig. 2(d).

APPENDIX D: EXTRACTION OF SPIN-ORBIT INTERACTION COEFFICIENTS FROM WEAK ANTILOCALIZATION BY COMBINATION OF WIRE MEASUREMENTS

To quantitatively evaluate Rashba and Dresselhaus SO coefficients, we focus on the different spin relaxation (i.e., magnetoconductance) behaviors between 2D and quasi-1D structures. In a 2D system near the PSH state, the collinear SO field stabilizes the spatial spin textures, while the imbalance between the linear field $[|\alpha| - (\beta_1 - \beta_3)]$ and cubic Dresselhaus field (β_3) causes DP spin relaxation and leads to WAL in the magnetoconductance. In contrast, in the quasi-1D system, the electron motion is laterally confined along the direction of the wire length, and the total SO field becomes unidirectional. Therefore, electron spins form the stable spatial textures and strongly suppress the spin relaxation, resulting in WL even in the case of the non-PSH state [70,71]. The additional application of in-plane magnetic field $\mathbf{B}_{\text{in}}$ breaks the unidirectional alignment of SO field $\mathbf{B}_{\text{SO}}$ and shows the anisotropic WL amplitude against the $\mathbf{B}_{\text{in}}$ angle, enabling us to directly extract the direction of SO field $\mathbf{B}_{\text{SO}}$ [67,68]. For a [010] wire, since the Rashba (linear Dresselhaus) field points perpendicular (parallel) to the wire direction, the ratio of α/β_1

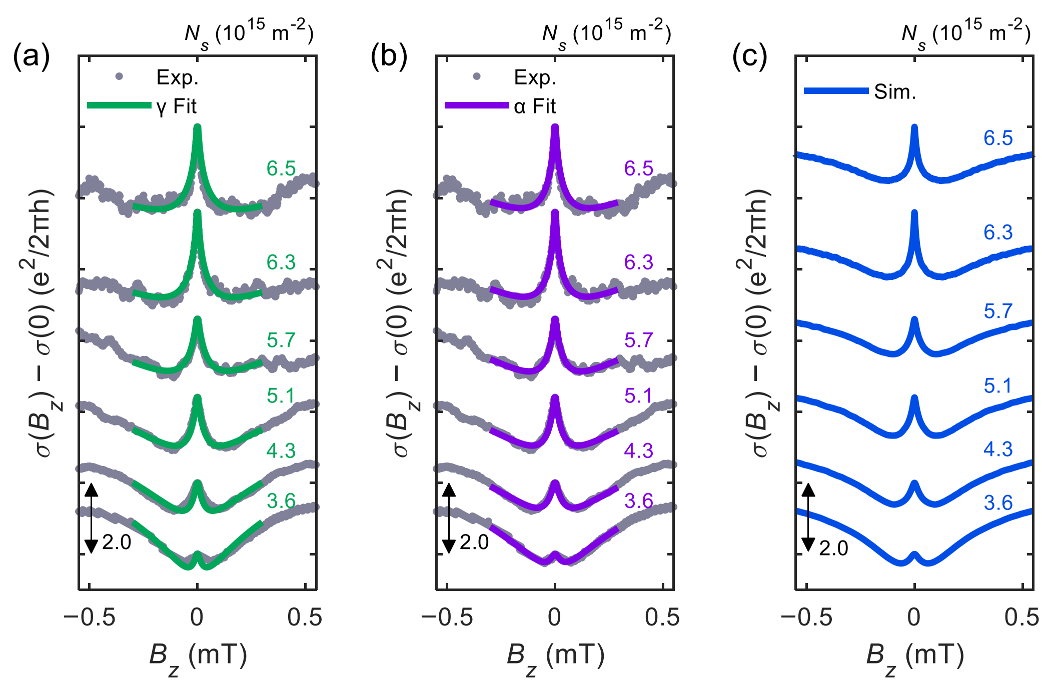

FIG. 12. (a) Measured weak antilocalization (WAL) signals and fits with single common γ and individually set L_ϕ as fit parameters. (b) Measured signals and fits with $|\alpha|$ and L_ϕ as free fit parameters. (c) The real-space simulated WAL curves corresponding to the experiments in each N_s.

can be obtained using Eq. (6). Once we determine the α/β_1 ratio which reduces the fitting parameter for WAL, we can quantify the full SO coefficients (α, β_1, β_3) by combining the results of 2D and quasi-1D measurements.

The flowchart of the extraction of full SO coefficients from WAL by combination of wire measurements is shown in Fig. 11. Firstly, we obtain $|\alpha|/\beta_1$ for all the measured carrier density N_s in the wire measurement. Next, we assume the linear dependence of $|\alpha|/\beta_1$ against N_s and obtain the relation of $|\alpha|/\beta_1 = R(N_s) = AN_S + C$ with constant values $A = 0.22 \times 10^{-15}$ m^2 and $C = 0.86$ [see Fig. 4(d)]. According to secured linear variation of $|\alpha|/\beta_1 = R(N_s) = AN_s + C$ in Fig. 4(d), we first replace $|\alpha|$ with $R(N_s)\beta_1$ so that we can rewrite all the SO coefficients in Eqs. (3a)–(3d) with only bulk Dresselhaus coefficient γ. Then, we fit all the WAL results with a single common γ as a fit parameter, while L_ϕ is individually set as a fit parameter for each N_s. As shown in Fig. 12(a), the fits (green solids) agree well with the experimental WAL signals (gray circles) in all measured N_s. This enables us to minimize the error of bulk Dresselhaus coefficient γ in each WAL curve and obtain the accurate value of $\gamma = -8.4\,\mathrm{eV}\,\text{Å}^3$ which is consistent with the previous results [17,56].

Next, to correct the small deviation of $|\alpha|$ from the linear assumption, we fit the WAL signals with $|\alpha|$ and L_ϕ as free fit parameters for each N_s, while keeping $\gamma = -8.4$ eV Å^3 as a constant. The fits (purple solids) and the experiments (gray circles) are shown in Fig. 12(b). According to calculated $\langle k_z^2\rangle = 2.7 \times 10^{16}$ m^{-2} as a virtually constant value on the present gate modulation and $k_\mathrm{F}^2 = 2\pi N_s$, all the SO coefficients ($|\alpha|$, β_1, β_3) can be fully evaluated, as summarized in Fig. 5(b).

Finally, we further perform the real-space simulation (Sawada and Koga [65] model) using the experimentally obtained SO coefficients ($|\alpha|$, β_1, β_3) and phase coherence length L_ϕ [Fig. 12(c)]. We reproduce the experimentally obtained WAL very well by the Sawada and Koga [65] model. Since the positions of conductance minimum in the WAL curve describing the SO strength are in qualitative agreement with the experiments for the entire N_s range, we conclude that the SO coefficients are successfully evaluated. It should be noted that because of the different interpretation of L_ϕ between the magnetoconductance correction expression [Eqs. (3a)–(3d)] and the real-space simulation (Sawada and Koga [65] model), the reduction of conductance near $B_z =$ 0 mT differs slightly from the experimental results.

[1] N. Nagaosa, J. Sinova, S. Onoda, A. H. MacDonald, and N. P. Ong, Anomalous Hall effect, Rev. Mod. Phys. **82**, 1539 (2010).

[2] Y. Taguchi, Y. Oohara, H. Yoshizawa, N. Nagaosa, and Y. Tokura, Spin chirality, Berry phase, and anomalous Hall effect in a frustrated ferromagnet, Science **291**, 2573 (2001).

[3] Y. Machida, S. Nakatsuji, Y. Maeno, T. Tayama, T. Sakakibara, and S. Onoda, Unconventional Anomalous Hall Effect Enhanced by a Noncoplanar Spin Texture in the Frustrated Kondo Lattice $Pr_2Ir_2O_7$, Phys. Rev. Lett. **98**, 057203 (2007).

[4] M. Heide, G. Bihlmayer, and S. Blügel, Dzyaloshinskii-Moriya interaction accounting for the orientation of magnetic domains in ultrathin films: Fe/W(110), Phys. Rev. B **78**, 140403(R) (2008).

[5] A. Thiaville, S. Rohart, É. Jué, V. Cros, and A. Fert, Dynamics of Dzyaloshinskii domain walls in ultrathin magnetic films, Europhys. Lett. **100**, 57002 (2012).

[6] S. Mühlbauer, B. Binz, F. Jonietz, C. Pfleiderer, A. Rosch, A. Neubauer, R. Georgii, and P. Böni, Skyrmion lattice in a chiral magnet, Science **323**, 915 (2009).

[7] C. Pappas, E. Lelièvre-Berna, P. Falus, P. M. Bentley, E. Moskvin, S. Grigoriev, P. Fouquet, and B. Farago, Chiral Paramagnetic Skyrmion-like Phase in MnSi, Phys. Rev. Lett. **102**, 197202 (2009).

[8] Y. Takeuchi, Y. Yamane, J-Y. Yoon, R. Itoh, B. Jinnai, S. Kanai, J. Ieda, S. Fukami, and H. Ohno, Chiral-spin rotation of non-collinear antiferromagnet by spin-orbit torque, Nat. Mater. **20**, 1364 (2021).

[9] J. Schliemann, J. C. Egues, and D. Loss, Nonballistic Spin-Field-Effect Transistor, Phys. Rev. Lett. **90**, 146801 (2003).

[10] B. A. Bernevig, J. Orenstein, and S-C. Zhang, Exact SU(2) Symmetry and Persistent Spin Helix in a Spin-Orbit Coupled System, Phys. Rev. Lett. **97**, 236601 (2006).

[11] J. D. Koralek, C. P. Weber, J. Orenstein, B. A. Bernevig, S.-C. Zhang, S. Mack, and D. D. Awschalom, Emergence of the persistent spin helix in semiconductor quantum wells, Nature (London) **458**, 610 (2009).

[12] M. P. Walser, C. Reichl, W. Wegscheider, and G. Salis, Direct mapping of the formation of a persistent spin helix, Nat. Phys. **8**, 757 (2012).

[13] M. Kohda, V. Lechner, Y. Kunihashi, T. Dollinger, P. Olbrich, C. Schönhuber, I. Caspers, V. V. Bel'kov, L. E. Golub, D. Weiss *et al.*, Gate-controlled persistent spin helix state in (In,Ga)As quantum wells, Phys. Rev. B **86**, 081306 (2012).

[14] P. Wenk, M. Kammermeier, and J. Schliemann, Conserved spin quantity in strained hole systems with Rashba and Dresselhaus spin-orbit coupling, Phys. Rev. B **93**, 115312 (2016).

[15] F. Dettwiler, J. Fu, S. Mack, P. J. Weigele, J. C. Egues, D. D. Awschalom, and D. M. Zumbühl, Stretchable Persistent Spin Helices in GaAs Quantum Wells, Phys. Rev. X **7**, 031010 (2017).

[16] J. Schliemann, Colloquium: Persistent spin textures in semiconductor nanostructures, Rev. Mod. Phys. **89**, 011001 (2017).

[17] M. Kohda and G. Salis, Physics and application of persistent spin helix state in semiconductor heterostructures, Semicond. Sci. Technol. **32**, 073002 (2017).

[18] M. Kammermeier, A. Seith, P. Wenk, and J. Schliemann, Persistent spin textures and currents in wurtzite nanowire-based quantum structures, Phys. Rev. B **101**, 195418 (2020).

[19] J. Fu, P. H. Penteado, M. O. Hachiya, D. Loss, and J. C. Egues, Persistent Skyrmion Lattice of Noninteracting Electrons with Spin-Orbit Coupling, Phys. Rev. Lett. **117**, 226401 (2016).

[20] Y. Oreg, G. Refael, and F. von Oppen, Helical Liquids and Majorana Bound States in Quantum Wires, Phys. Rev. Lett. **105**, 177002 (2010).

[21] R. M. Lutchyn, J. D. Sau, and S. Das Sarma, Majorana Fermions and a Topological Phase Transition in Semiconductor-Superconductor Heterostructures, Phys. Rev. Lett. **105**, 077001 (2010).

[22] Z. Li, F. Marsiglio, and J. P. Carbotte, Vanishing of interband light absorption in a persistent spin helix state, Sci. Rep. **3**, 2828 (2013).

[23] Y. A. Bychkov and E. I. Rashba, Oscillatory effects and the magnetic susceptibility of carriers in inversion layers, J. Phys. C: Solid State Phys. **17**, 6039 (1984).

[24] G. Dresselhaus, Spin-orbit coupling effects in zinc blende structures, Phys. Rev. **100**, 580 (1955).

[25] M. I. D'yakonov and V. I. Perel', Spin relaxation of conduction electrons in noncentrosymmetric semiconductors, Sov. Phys. Solid State **13**, 3023 (1972).

[26] T. D. Stanescu and V. Galitski, Spin relaxation in a generic two-dimensional spin-orbit coupled system, Phys. Rev. B **75**, 125307 (2007).

[27] P. Wenk and S. Kettemann, Dimensional dependence of weak localization corrections and spin relaxation in quantum wires with Rashba spin-orbit coupling, Phys. Rev. B **81**, 125309 (2010).

[28] L. Yang, J. Orenstein, and D.-H. Lee, Random walk approach to spin dynamics in a two-dimensional electron gas with spin-orbit coupling, Phys. Rev. B **82**, 155324 (2010).

[29] M. C. Lüffe, J. Kailasvuori, and T. S. Nunner, Relaxation mechanisms of the persistent spin helix, Phys. Rev. B **84**, 075326 (2011).

[30] G. Salis, M. P. Walser, P. Altmann, C. Reichl, and W. Wegscheider, Dynamics of a localized spin excitation close to the spin-helix regime, Phys. Rev. B **89**, 045304 (2014).

[31] D. Iizasa, M. Kohda, U. Zülicke, J. Nitta, and M. Kammermeier, Enhanced longevity of the spin helix in low-symmetry quantum wells, Phys. Rev. B **101**, 245417 (2020).

[32] J. Ishihara, Y. Ohno, and H. Ohno, Direct imaging of gate-controlled persistent spin helix state in a modulation-doped GaAs/AlGaAs quantum well, Appl. Phys. Express **7**, 013001 (2014).

[33] Y. Kunihashi, H. Sanada, H. Gotoh, K. Onomitsu, M. Kohda, J. Nitta, and T. Sogawa, Drift transport of helical spin coherence with tailored spin-orbit interactions, Nat. Commun. **7**, 10722 (2016).

[34] M. Luengo-Kovac, F. C. D. Moraes, G. J. Ferreira, A. S. L. Ribeiro, G. M. Gusev, A. K. Bakarov, V. Sih, and F. G. G. Hernandez, Gate control of the spin mobility through the modification of the spin-orbit interaction in two-dimensional systems, Phys. Rev. B **95**, 245315 (2017).

[35] F. Passmann, S. Anghel, C. Ruppert, A. D. Bristow, A. V. Poshakinskiy, S. A. Tarasenko, and M. Betz, Dynamical formation and active control of persistent spin helices in III-V and II-VI quantum wells, Semicond. Sci. Technol. **34**, 093002 (2019).

[36] Y. S. Chen, S. Fält, W. Wegscheider, and G. Salis, Unidirectional spin-orbit interaction and spin-helix state in a (110)-oriented GaAs/(Al,Ga)As quantum well, Phys. Rev. B **90**, 121304(R) (2014).

[37] K. Yoshizumi, A. Sasaki, M. Kohda, and J. Nitta, Gate-controlled switching between persistent and inverse persistent spin helix states, Appl. Phys. Lett. **108**, 132402 (2016).

[38] P. J. Weigele, D. C. Marinescu, F. Dettwiler, J. Fu, S. Mack, J. C. Egues, D. D. Awschalom, and D. M. Zumbühl, Symmetry breaking of the persistent spin helix in quantum transport, Phys. Rev. B **101**, 035414 (2020).

[39] M. Kammermeier, T. Saito, D. Iizasa, U. Zülicke, and M. Kohda, Reliable modeling of weak antilocalization for accurate spin-lifetime extraction, Phys. Rev. B **104**, 235430 (2021).

[40] A. E. Hansen, M. T. Björk, C. Fasth, C. Thelander, and L. Samuelson, Spin relaxation in InAs nanowires studied by tunable weak antilocalization, Phys. Rev. B **71**, 205328 (2005).

[41] R. L. Kallaher, J. J. Heremans, N. Goel, S. J. Chung, and M. B. Santos, Spin-orbit interaction determined by antilocalization in an InSb quantum well, Phys. Rev. B **81**, 075303 (2010).

[42] Z. Lei, E. Cheah, K. Rubi, M. E. Bal, C. Adam, R. Schott, U. Zeitler, W. Wegscheider, T. Ihn, and K. Ensslin, High-quality two-dimensional electron gas in undoped InSb quantum wells, Phys. Rev. Res. **4**, 013039 (2022).

[43] N. Yamaguchi and F. Ishii, Strain-induced large spin splitting and persistent spin helix at $LaAlO_3/SrTiO_3$ interface, Appl. Phys. Express **10**, 123003 (2017).

[44] M. A. U. Absor, F. Ishii, H. Kotaka, and M. Saito, Persistent spin helix on a wurtzite ZnO(1010) surface: first-principles density-functional study, Appl. Phys. Express **8**, 073006 (2015).

[45] M. A. U. Absor and F. Ishii, Doping-induced persistent spin helix with a large spin splitting in monolayer SnSe, Phys. Rev. B **99**, 075136 (2019).

[46] M. A. U. Absor and F. Ishii, Intrinsic persistent spin helix state in two-dimensional group-IV monochalcogenide *MX* monolayers ($M =$ Sn or Ge and $X =$ S, Se, or Te), Phys. Rev. B **100**, 115104 (2019).

[47] H. Lee, J. Im, and H. Jin, Emergence of the giant out-of-plane Rashba effect and tunable nanoscale persistent spin helix in ferroelectric SnTe thin films, Appl. Phys. Lett. **116**, 022411 (2020).

[48] J. Sławińska, F. T. Cerasoli, P. Gopal, M. Costa, S. Curtarolo, and M. B. Nardelli, Ultrathin SnTe films as a route towards all-in-one spintronics devices, 2D Mater. **7**, 025026 (2020).

[49] S. A. Sasmito, M. Anshory, I. Jihad, and M. A. U. Absor, Reversible spin textures with giant spin splitting in two-dimensional Ga*XY* ($X =$ Se, Te; $Y =$ Cl, Br, I) compounds for a persistent spin helix, Phys. Rev. B **104**, 115145 (2021).

[50] L. L. Tao and E. Y. Tsymbal, Persistent spin texture enforced by symmetry, Nat. Commun. **9**, 2763 (2018).

[51] C. Autieri, P. Barone, J. Sławi´nska, and S. Picozzi, Persistent spin helix in Rashba-Dresselhaus ferroelectric $CsBiNb_2O_7$, Phys. Rev. Mater. **3**, 084416 (2019).

[52] L. L. Tao and E. Y. Tsymbal, Perspectives of spin-textured ferroelectrics, J. Phys. D: Appl. Phys. **54**, 113001 (2021).

[53] X.-Z. Lu and J. M. Rondinelli, Discovery principles and materials for symmetry-protected persistent spin textures with long spin lifetimes, Matter **3**, 1211 (2020).

[54] J. Ji, F. Lou, R. Yu, J. S. Feng, and H. J. Xiang, Symmetry-protected full-space persistent spin texture in two-dimensional materials, Phys. Rev. B **105**, L041404 (2022).

[55] L. Zhang, J. Jian, C. Multunas, C. Ming, Z. Chen, Y. Hu, Z. Lu, S. Pendse, R. Jia, M. Chandra *et al.*, Room-temperature electrically switchable spin-valley coupling in a van der Waals ferroelectric halide perovskite with persistent spin helix, Nat. Photon. **16**, 529 (2022).

[56] T. Saito, A. Aoki, J. Nitta, and M. Kohda, Simultaneous evaluation of drift- and diffusion-induced spin-orbit fields in a (001) GaAs/AlGaAs two-dimensional electron gas, Appl. Phys. Lett. **115**, 052402 (2019).

[57] B. L. Altshuler, A. G. Aronov, A. I. Larkin, and D. E. Khmelnitskii, Anomalous magnetoresistance in semiconductors, Sov. Phys. JETP **54**, 411 (1981) [Zh. Eksp. Teor. Fiz. **81**, 768 (1981)].

[58] S. V. Iordanskii, Yu. B. Lyanda-Geller, and G. E. Pikus, Weak localization in quantum wells with spin-orbit interaction, JETP Lett. **60**, 206 (1994) [Pis'ma Zh. Eksp. Teor. Fiz. **60**, 199 (1994)].

[59] F. G. Pikus and G. E. Pikus, Conduction-band spin splitting and negative magnetoresistance in A_3B_5 heterostructures, Phys. Rev. B **51**, 16928 (1995).

[60] W. Knap, C. Skierbiszewski, A. Zduniak, E. Litwin-Staszewska, D. Bertho, F. Kobbi, J. L. Robert, G. E. Pikus, F. G. Pikus, S. V. Iordanskii *et al.*, Weak antilocalization and spin precession in quantum wells, Phys. Rev. B **53**, 3912 (1996).

[61] T. Hassenkam, S. Pedersen, K. Baklanov, A. Kristensen, C. B. Sorensen, P. E. Lindelof, F. G. Pikus, and G. E. Pikus, Spin splitting and weak localization in (110) $\mathrm{GaAs/Al}_x\mathrm{Ga}_{1-x}\mathrm{As}$ quantum wells, Phys. Rev. B **55**, 9298 (1997).

[62] M. Kammermeier, P. Wenk, and J. Schliemann, Control of Spin Helix Symmetry in Semiconductor Quantum Wells by Crystal Orientation, Phys. Rev. Lett. **117**, 236801 (2016).

[63] D. C. Marinescu, P. J. Weigele, D. M. Zumbühl, and J. C. Egues, Closed-Form Weak Localization Magnetoconductivity in Quantum Wells with Arbitrary Rashba and Dresselhaus Spin-Orbit Interactions, Phys. Rev. Lett. **122**, 156601 (2019).

[64] A. G. Mal'shukov, K. A. Chao, and M. Willander, Magnetoresistance of a weakly disordered III-V semiconductor quantum well in a magnetic field parallel to interfaces, Phys. Rev. B **56**, 6436 (1997).

[65] A. Sawada and T. Koga, Universal modeling of weak antilocalization corrections in quasi-two-dimensional electron systems using predetermined return orbitals, Phys. Rev. E **95**, 023309 (2017).

[66] J. Nitta, T. Akazaki, H. Takayanagi, and T. Enoki, Gate Control of Spin-Orbit Interaction in an Inverted $\mathrm{In}_{0.53}\mathrm{Ga}_{0.47}\mathrm{As/In}_{0.52}\mathrm{Al}_{0.48}\mathrm{As}$ Heterostructure, Phys. Rev. Lett. **78**, 1335 (1997).

[67] A. Sasaki, S. Nonaka, Y. Kunihashi, M. Kohda, T. Bauernfeind, T. Dollinger, K. Richter, and J. Nitta, Direct determination of spin-orbit interaction coefficients and realization of the persistent spin helix symmetry, Nat. Nanotechnol. **9**, 703 (2014).

[68] T. Nishimura, K. Yoshizumi, T. Saito, D. Iizasa, J. Nitta, and M. Kohda, Full spin-orbit coefficient in III-V semiconductor wires based on the anisotropy of weak localization under in-plane magnetic field, Phys. Rev. B **103**, 094412 (2021).

[69] T. J. Thornton, M. L. Roukes, and A. Scherer, and B. P. Van de Gaag, Boundary Scattering in Quantum Wires, Phys. Rev. Lett. **63**, 2128 (1989).

[70] P. Altmann, M. Kohda, C. Reichl, W. Wegscheider, and G. Salis, Transition of a two-dimensional spin mode to a helical state by lateral confinement, Phys. Rev. B **92**, 235304 (2015).

[71] Th. Schäpers, V. A. Guzenko, M. G. Pala, U. Zülicke, M. Governale, J. Knobbe, and H. Hardtdegen, Suppression of weak antilocalization in $\mathrm{Ga}_x\mathrm{In}_{1-x}\mathrm{As/InP}$ narrow quantum wires, Phys. Rev. B **74**, 081301(R) (2006).

[72] M. Scheid, M. Kohda, Y. Kunihashi, K. Richter, and J. Nitta, All-Electrical Detection of the Relative Strength of Rashba and Dresselhaus Spin-Orbit Interaction in Quantum Wires, Phys. Rev. Lett. **101**, 266401 (2008).

[73] S. Hikami, A. I. Larkin, and Y. Nagaoka, Spin-orbit interaction and magnetoresistance in the two dimensional random system, Prog. Theor. Phys. **63**, 707 (1980).

[74] T. Koga, J. Nitta, and M. van Veenhuizen, Ballistic spin interferometer using the Rashba effect, Phys. Rev. B **70**, 161302(R) (2004).